




Functional hydrogels promote chronic infectious wound healing by re-rousing macrophage M1 and inducing bacterial copper-like death

Chao Xiang^{a,b,1}, Chaoyu Pu^{a,b,1}, XueMei Zhong^{c,1}, Yong Wang^b, Weiyong Song^b, Xingkuan Wang^b, Kemiao Chen^d, Kai Li^{a,*}, Yue Luo^{b,**}, Ke Jiang^{b,***}, Dianming Jiang^{a,****} 

^a Department of Orthopedics, The Third Affiliated Hospital of Chongqing Medical University, 401120, Chongqing, China

^b Department of Orthopedics, The Affiliated Hospital of North Sichuan Medical College, 637000, Nanchong, China

^c School of Clinical Medicine, Chongqing Medical and Pharmaceutical College, Chongqing, 401331, China

^d Chongqing Medical University, 401120, Chongqing, China

ARTICLE INFO

Keywords:

Chronic infectious wounds
Hydrogels
Microspheres
Immune regulation
Macrophages

ABSTRACT

Traditional antibiotics are often ineffective against biofilm-associated infections, and biofilm-induced macrophage immune evasion directly halts the wound healing process. Disrupting biofilms and regulating macrophage immune functions are critical to improving wound healing. In this study, we synthesized g-C₃N₄ with peroxidase (POD) enzyme activity via thermal polymerization and copper alginate microspheres (CAM) via gas cutting. These were co-encapsulated into GelMA hydrogels to form a functionalized wound repair system (GelMA/CAM@g-C₃N₄) with both anti-biofilm and local immune microenvironment remodeling capabilities. In vitro, this system exhibited excellent biocompatibility and promoted endothelial cell migration, vascular formation, and CD31 expression. It also polarized macrophages toward the M1 phenotype, restoring their pro-inflammatory functions, upregulating inflammatory cytokines (IL-1, IL-6, TNF-α), and inhibiting *Staphylococcus aureus* and *Escherichia coli*. In vivo, the system suppressed *S. aureus* growth, promoted angiogenesis and collagen deposition, and reshaped the pathological microenvironment to achieve wound repair and regeneration. Conclusions: This system offers a new therapeutic strategy for chronic infectious wounds.

1. Introduction

Chronic wounds are those that fail to restore anatomical and functional integrity within three months post-injury, affecting approximately 1–2 % of the global population [1]. Infection is considered one of the key factors contributing to chronic wounds, as it impedes the healing process, increases wound pain, places a significant economic burden on healthcare systems, and lowers patients' quality of life [2]. Over the past few decades, many new antibiotics have been developed, and antibiotics have long been considered the ultimate solution for biofilm-related bacterial infections in humans [3]. Unfortunately, the formation of biofilms is highly resistant to antibiotics, making infections increasingly challenging [4–6]. Biofilms are complex bacterial aggregates composed of bacterial cells, extracellular polymeric substances (EPS), and other

microorganisms, which aid in bacterial colonization, enhance resistance to antimicrobial agents, evade host immunity, and facilitate inter-bacterial signaling within the community [7–9]. *Staphylococcus aureus* is the most common organism isolated from human chronic wounds [10]. Currently, clinical biofilm treatments involve removing infected tissue and using antibiotics in combination. However, this approach has several drawbacks, including invasive procedures, uncertain efficacy, and high treatment costs [11,12]. Therefore, there is an urgent need to develop alternative therapeutic platforms to control pathogenic biofilm-associated infections.

The normal wound healing process progresses through four overlapping cascades: hemostasis, inflammation, proliferation, and remodeling [13]. Macrophages are the first line of defense against pathogens and possess high plasticity, rapidly adapting to the complex

* Corresponding author.

** Corresponding author.

*** Corresponding author.

**** Corresponding author.

E-mail addresses: lixiangkai58@163.com (K. Li), lyhuaxi@126.com (Y. Luo), jiangke2010@nsmc.edu.cn (K. Jiang), 201296@hospital.cqmu.edu.cn (D. Jiang).

¹ These authors contributed equally to this work.

microenvironment triggered by tissue infection or inflammation through polarization. M1 macrophages recognize, phagocytose, and kill invading bacteria, and after completing their pro-inflammatory mission, they polarize to the M2 phenotype, which promotes tissue repair. Macrophages are key regulatory factors in wound healing and tissue regeneration, ultimately leading to wound healing [14–17]. However, in chronic wounds, mature biofilms have dense EPS, which makes it difficult for macrophages to phagocytose, leading to “frustrated phagocytosis” [18]. Reactive oxygen species (ROS) have been shown to promote M1 macrophage polarization (pro-inflammatory and bactericidal) and activate macrophage oxidative bursts, acidification, and enzyme-mediated phagocytosis, including phagolysosome formation, to eliminate invading bacteria [19,20]. Thus, reactivating the pro-inflammatory function of M1 macrophages in chronically infected wounds, reversing the immune environment, and reshaping the “physiological healing process” of the wound through ROS are considered promising therapeutic strategies for chronically infected wounds caused by biofilm-induced immune evasion [8,21,22].

In the past thirty years, significant progress has been made in the research of the biological functions and physical properties of nanomaterials for applications such as anti-biofilm and anti-tumor fields [23–25]. Novel nanomaterials with high peroxidase (POD)-like activity, such as noble metals, iron-based nanomaterials, transition metal dichalcogenides, and polyoxometalates, are known [19,26,27]. Unfortunately, these nanomaterials still have limitations, such as inherent cytotoxicity and oxidative stress under low H_2O_2 concentrations, which can damage cellular function. Photocatalytic antibacterial therapy is an effective strategy relying on external stimuli. Due to its controllability, safety, and non-invasiveness, it has garnered increasing attention over the past few decades, with many photosensitizers developed. The metal-free polymer two-dimensional nanomaterial graphitic carbon nitride ($g-C_3N_4$) is particularly attractive as a photosensitizer for non-antibiotic antibacterial applications due to its abundance, ease of synthesis, appropriate band structure, high stability, and low toxicity [28,29]. More importantly, $g-C_3N_4$ has been recently shown to generate micromolar concentrations of H_2O_2 continuously, which can successfully combat established biofilms [30]. However, although the generated H_2O_2 can fight biofilms, a single antibacterial mechanism is insufficient to completely prevent biofilm formation or provide long-term antibacterial effects at the wound site. Metal nanoparticles are known for their non-specific bacterial toxicity mechanisms, which prevent bacteria from developing resistance and broaden their antibacterial activity [31]. Copper is a classical antimicrobial metal that has been widely used to combat Gram-negative, Gram-positive, and fungal infections due to its recognized antibacterial and pro-angiogenic properties, making it essential in wound healing [32]. Studies have shown that copper ions exert antimicrobial effects through various mechanisms, including altering membrane permeability, DNA structure, metabolism, and enzyme activity [33,34]. Thus, we aim to incorporate antimicrobial ions to achieve synergistic antibacterial effects. Alginate is a naturally occurring anionic polysaccharide extracted from brown algae, which forms stable complex structures upon contact with divalent cations (such as calcium and copper) and promotes the release of these ions in acidic conditions [35]. We developed copper alginate microspheres (CAM) for slow release, achieving long-term antibacterial effects for chronically infected wounds.

To ensure the therapeutic effects of the composite system of nanomaterials and metal nanoparticles, and considering its potential as an ideal medium for wound healing, we further encapsulated the system in hydrogels, which are widely used for wound treatment due to their excellent hydrophilicity, drug-loading capacity, and sustained release properties [36]. Gelatin methacrylate (GelMA) is a gelatin derivative and denatured collagen product known for its excellent solubility and low antigenicity. The incorporation of the Arg-Gly-Asp (RGD) sequence enhances biological interactions between cells and the GelMA scaffold, making GelMA an ideal biomaterial for wound healing, morphogenesis,

and tissue restoration [37].

In summary, based on the pathogenesis of biofilm formation and macrophage immune evasion in chronic infected wounds, we developed a functionalized hydrogel microsphere system. This system combats bacterial biofilms through ROS and reactivates the M1 phenotype of macrophages, while the slow release of antimicrobial metal ions provides long-lasting antibacterial effects and promotes angiogenesis, reshaping the physiological repair process of the wound. We synthesized $g-C_3N_4$ with POD enzyme activity through thermal polymerization and CAM via a gas-cutting method, and finally encapsulated $g-C_3N_4$ and CAM in GelMA hydrogel to construct a chronic infected wound healing system (GelMA/CAM@ $g-C_3N_4$) (Scheme 1). This system demonstrated excellent biocompatibility in vitro, promoted endothelial cell migration and vascular tube formation, reactivated M1 macrophages, and enhanced the expression of inflammatory cytokines (IL-1, IL-6, TNF- α). It significantly inhibited *Staphylococcus aureus* and *Escherichia coli*. Gene expression analysis showed that the system induced copper-like death of *S. aureus* by downregulating metabolic pathways such as glycolysis, oxidative phosphorylation, purine, and pyrimidine. In vivo, the system inhibited *S. aureus* growth, reactivated M1 macrophages by day 3, polarized macrophages to the M2 phenotype by day 7, promoted angiogenesis, and enhanced collagen deposition. This system provides a novel approach for treating biofilm-infected wounds and lays a foundation for addressing biofilm-related infectious diseases.

2. Methods and methods

2.1. Experimental materials

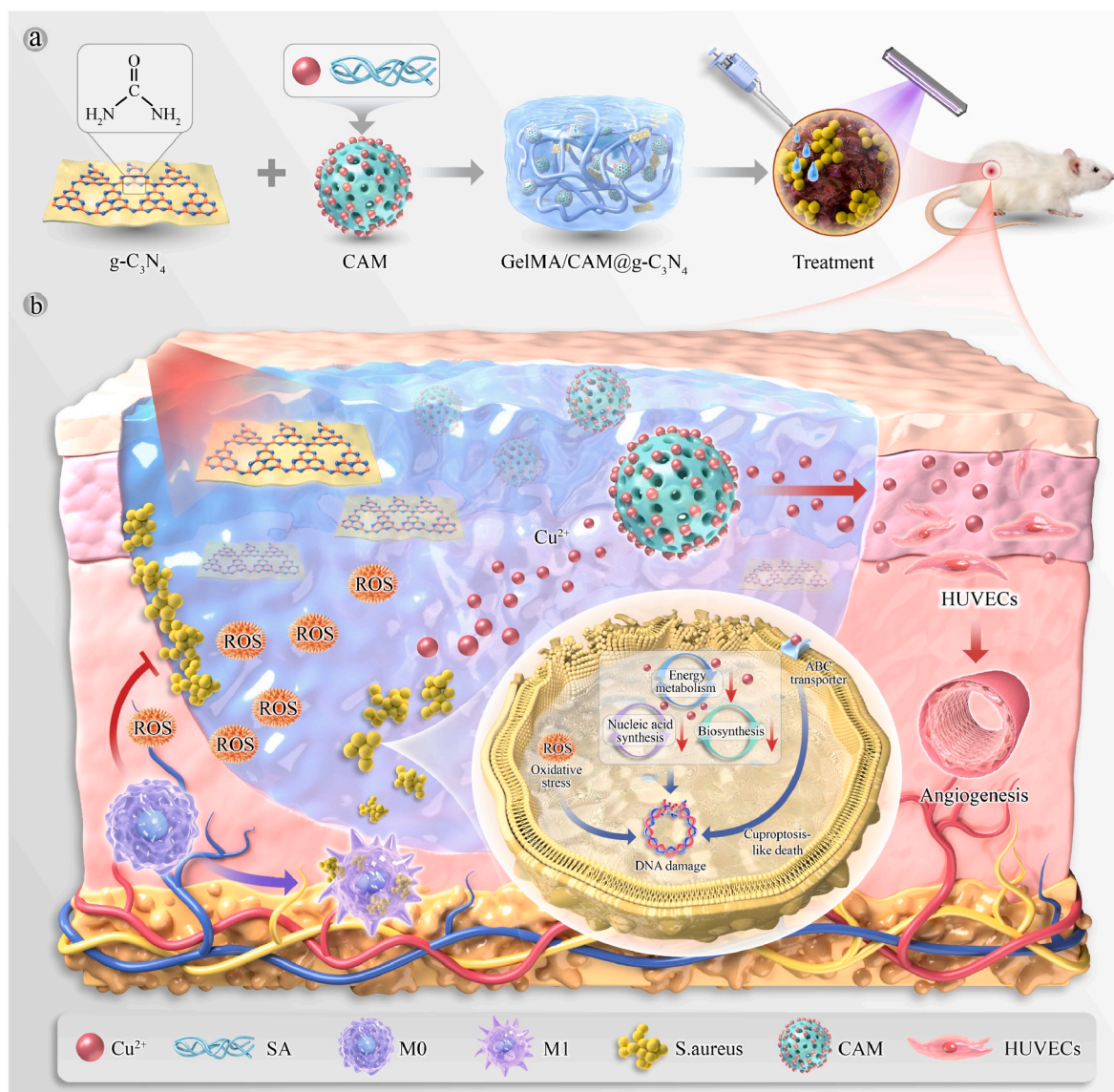
Urea, sodium alginate, copper chloride, and gelatin were purchased from Aladdin Reagent (Shanghai, China); CCK-8 was obtained from Biyuntian Biotechnology (Shanghai, China); dialysis bags (8000D) were purchased from Macklin Biochemical Co., Ltd. (Shanghai, China); the bacterial live-dead staining kit was purchased from Maokang Biotechnology Co., Ltd. (Shanghai, China); Matrigel was obtained from Gelcon BioTech (Shanghai, China); photo-initiator and methacrylic anhydride were purchased from Sigma-Aldrich Trading Co., Ltd. (Shanghai, China); DAPI was purchased from Wuhan Boster Biological Technology Ltd.; CD31 antibody, CD86 antibody, and CD206 antibody were purchased from Affinity Biosciences (Jiangsu, China); the DCFH-DA probe was purchased from Uelandy Biotechnology (Suzhou, China); FITC phalloidin was purchased from Sagon Biotech (Guangzhou, China); DMEM culture medium and fetal bovine serum were purchased from Gibco (USA).

2.2. Experimental equipment

The following equipment was used: intelligent biochemical incubator (SPX-280Y, Ningbo Ke sheng Laboratory Instruments Co., Ltd., China), thermostatic shaker (THZ-82, Guohua Instruments Co., Ltd., China), high-speed centrifuge (5804R, Eppendorf China Co., Ltd., China), microbiological workstation (HCB-900V, Haier Biomedical Co., Ltd., China), PCR machine (T100, Bio-Rad, USA), transmission electron microscope (HT7700, Japan), biosafety cabinet (1374, Thermo Fisher Scientific, Suzhou, China), high-speed centrifuge (5702, Eppendorf International Trading Co., Ltd., Shanghai, China), confocal microscope (Olympus, Japan), UV-Vis spectrophotometer (Shimadzu UV-2700, Japan), microplate reader (Bio-Rad, USA), fluorescence inverted microscope (CKX53, Japan), and magnetic stirrer (MS-H-Pro, Dragonlab Instrument Co., Ltd., Beijing, China).

2.3. Synthesis of $g-C_3N_4$ and H_2O_2 generation

10 g of urea was accurately weighed and dissolved completely in 30 mL of deionized water. The solution was then transferred to a crucible at 60 °C and continued to be dried for 8 h to obtain a white crystalline



Scheme 1. Schematic illustration of the construction of the GelMA/CAM@g-C₃N₄ system and its application to infected wounds.

solid. This solid was subsequently transferred to a muffle furnace. It was calcined at a heating rate of 5 °C/min until the temperature reached 600 °C, after which the calcination was continued for 2 h. The resulting light yellow solid was g-C₃N₄. Its morphology was observed using TEM, its elemental composition and chemical bonds were confirmed by XPS, and its crystal structure was analyzed by XRD.

Initially, standard H₂O₂ solutions (0, 0.05, 0.1, 0.2, 0.4, 0.8 mmol/L) were reacted with an H₂O₂ assay kit for 10 min. The absorbance was measured using a microplate reader at 405 nm to establish a standard curve. Different concentrations of g-C₃N₄ (50, 100, 200 µg/mL) were prepared and measured at various time points (0, 0.5, 1, 1.5, 2 h) under visible light using the H₂O₂ assay kit. The generation of H₂O₂ was calculated based on the standard curve.

2.4. Synthesis and characterization of copper alginate microspheres (CAM)

Copper alginate microspheres were synthesized by air cutting. First, 10 g of sodium alginate was weighed and dissolved in deionized water to prepare a 0.5 % sodium alginate solution. Then, 1 g of CuCl₂ was weighed and dissolved in 99 mL of deionized water under ultrasonication to prepare a 1 % CuCl₂ solution. The sodium alginate solution

was loaded into a 10 mL syringe and pushed into a microfluidic system at a rate of 5 mL/h, where nitrogen (0.1 mpa) was used to cut the microspheres, which were then dropped into the CuCl₂ solution for cross-linking. The copper alginate microspheres were stored at 4 °C. Their morphology and structure were observed using an optical microscope, particle size was measured by Image J, and their microstructure and elemental composition were analyzed by SEM.

2.5. Synthesis of GelMA and combination with copper alginate microspheres

First, a carbonate buffer was prepared by dissolving 0.3427 g Na₂CO₃ and 3.0915 g NaHCO₃ in 200 mL of deionized water. Then, 20 g of gelatin was dispersed in 200 mL of carbonate buffer (pH 9.0) and heated in a 50 °C oil bath until completely dissolved to make a 10 % gelatin solution. Next, 2 mL of MA (methacrylic anhydride) was slowly added to the gelatin solution using a syringe pump at a rate of 0.2 mL/min while protecting from light. After the addition, the reaction continued for 3 h in the oil bath. Then, 100 mL of PBS was added to terminate the reaction. The mixture was centrifuged (7000 rpm, 15 min) to remove unreacted MA. The GelMA was then placed in a dialysis bag (MWCO 3500) and dialyzed at 38 °C for 2 days. Finally, the GelMA was lyophilized and

stored at -20°C .

A suitable amount of GelMA was dissolved in PBS to prepare a 5 % GelMA solution, to which 0.25 % LAP (photo-initiator) was added by mass-volume ratio. Copper alginate microspheres and $\text{g-C}_3\text{N}_4$ were then added to the solution, and the mixture was exposed to UV light for 30 s. The morphology of the GelMA hydrogel containing microspheres and $\text{g-C}_3\text{N}_4$ was observed by SEM after lyophilization.

2.6. Adhesion experiment of functionalized hydrogels

The functionalized hydrogels were prepared as described above and applied evenly to glass slides. Rat hearts, livers, spleens, lungs, and kidneys were individually placed on the hydrogel-coated slides. The adhesion was evaluated by visual observation and photographic documentation.

2.7. Swelling property test of functionalized hydrogels

Different systems of functionalized hydrogels were prepared (GelMA (G), GelMA/ $\text{g-C}_3\text{N}_4$ (G-g), GelMA/CAM (G-C), GelMA/CAM@ $\text{g-C}_3\text{N}_4$ (G-C-g)), lyophilized, and weighed (A_1). The lyophilized hydrogels were then soaked in 50 mL PBS (pH 7.4) at 37°C for 24 h. After soaking, the hydrogels were blotted dry with filter paper and weighed again (A_2). The swelling ratio was calculated using the following formula:

$$\text{Swelling ratio} = \frac{A_2 - A_1}{A_1} \times 100 \% \quad (1)$$

Each experiment was repeated three times.

2.8. Drug release curve of functionalized hydrogels

A UV standard curve for $\text{g-C}_3\text{N}_4$ was established using UV spectroscopy. Specifically, different concentrations of $\text{g-C}_3\text{N}_4$ (1000, 500, 250, 125, 62.25, 31.125 $\mu\text{g/mL}$) were prepared, and the UV absorption peaks were measured to create the standard curve.

To obtain the drug release curve of $\text{g-C}_3\text{N}_4$, GelMA/ $\text{g-C}_3\text{N}_4$ hydrogels were prepared. A 10 mL hydrogel was placed in 200 mL PBS and incubated in a thermostatic shaker (37°C ; 70 rpm). At specific time points (0, 1, 2, 4, 6, 8, 10, 12, 24, 36, 48, 72 h), 2 mL of release medium was removed for UV analysis, and the release amount was calculated based on the standard curve. The following formula was used to calculate the release rate:

$$\text{Release rate} = \frac{A_2}{A_1} \times 100 \% \quad (2)$$

where A_1 was the total amount of the drug, and A_2 was the amount of drug released at a specific time point.

Similarly, the copper ion release curve was obtained. A copper ion detection kit was used to establish a standard curve based on standard copper ion concentrations (0, 10, 20, 30, 40, 50 $\mu\text{g/mL}$) measured with a microplate reader. GelMA/CAM hydrogels were prepared, and a 10 mL hydrogel was placed in 200 mL PBS. Samples were taken at specified times (0, 1, 2, 4, 6, 8, 10, 12, 24, 36, 48, 72 h) for copper ion analysis, and the release amount was calculated according to the standard curve. The release rate was calculated using the same formula as above.

2.9. CCK-8 assay to evaluate the biocompatibility of $\text{g-C}_3\text{N}_4$ and copper ions

The biocompatibility of $\text{g-C}_3\text{N}_4$ was evaluated using a CCK-8 assay. Human umbilical vein endothelial cells (HUVECs) at a density of 5×10^3 cells were seeded into a 96-well plate and treated with DMEM (serum-free) medium containing different concentrations of $\text{g-C}_3\text{N}_4$ (0, 50, 100, 150, 200, 250 $\mu\text{g/mL}$) for 24 h. After incubation, 100 μL of CCK-8 solution was added to each well and further incubated at 37°C for 0.5 h. The absorbance at 450 nm was measured using a microplate reader, and

cell viability was calculated. This same method was used to evaluate the biocompatibility of $\text{g-C}_3\text{N}_4$ in RAW264.7 cells, with the experiment repeated three times.

Next, the biocompatibility of copper ions was assessed using the CCK-8 assay. HUVECs at a density of 5×10^3 cells were seeded into a 96-well plate and treated with DMEM (serum-free) medium containing various concentrations of copper ions (0, 10, 20, 30, 40, 50 $\mu\text{g/mL}$) for 24 h. After incubation, 100 μL of CCK-8 solution was added to each well and further incubated at 37°C for 0.5 h. The absorbance at 450 nm was measured using a microplate reader to calculate cell viability. This method was similarly applied to evaluate the biocompatibility of $\text{g-C}_3\text{N}_4$ in RAW264.7 cells, with the experiment repeated three times.

2.10. Live/dead staining of functionalized hydrogels

To assess the biocompatibility of different functionalized hydrogels, an indirect extraction method was used. Functionalized hydrogel systems, including PBS, GelMA, GelMA/ $\text{g-C}_3\text{N}_4$, GelMA/CAM, and GelMA/CAM@ $\text{g-C}_3\text{N}_4$, were incubated with DMEM medium at a ratio of 0.2 g/mL in accordance with national standards (GB/T 16886.5–2017) for 24 h to obtain hydrogel extracts. HUVECs at a density of 5×10^4 cells were seeded into a 24-well plate and treated with different hydrogel extracts for 24 h. Live/dead staining solution was added, followed by three washes with PBS. The cells were observed and photographed using an inverted fluorescence microscope. The experiment was repeated three times.

2.11. Cell migration assay

HUVECs at a density of 1×10^5 cells were seeded into a 6-well plate and cultured in a CO_2 incubator (37°C , 5 % CO_2) until they reached confluency. A pipette tip was used to scratch the cell monolayer, creating a narrow wound gap. The cells were then incubated with extracts of PBS, GelMA, GelMA/ $\text{g-C}_3\text{N}_4$, GelMA/CAM, or GelMA/CAM@ $\text{g-C}_3\text{N}_4$ in serum-free medium. The wound area was photographed using Cap Studio software, and Image J was used to analyze the wound area. The cell migration rate was calculated using the following formula:

$$\text{Migration rate} = \frac{A_1 - A_2}{A_1} \times 100 \% \quad (3)$$

Where A_1 is the wound area at $t = 0$ h, and A_2 is the wound area at the specified time.

2.12. Tube formation assay

HUVECs at a density of 1×10^5 cells were seeded into a 6-well plate. Once attached, the cells were incubated with serum-free DMEM extracts of PBS, GelMA, GelMA/ $\text{g-C}_3\text{N}_4$, GelMA/CAM, or GelMA/CAM@ $\text{g-C}_3\text{N}_4$ for 24 h. Matrigel was stored at 4°C overnight and diluted with DMEM at a 2:1 ratio. After thoroughly mixing, 75 μL of Matrigel was added to each well of a 96-well plate and allowed to solidify at 37°C for 30 min. HUVECs were then digested with trypsin and seeded into each well of the 96-well plate at a density of 3×10^4 cells per well. After 12 h, the formation of tube-like structures was observed under an inverted fluorescence microscope in Brightfield. The number of nodes and tube formation were quantified using Image J. The experiment was repeated three times.

2.13. Promotion of CD31 expression in HUVECs by functionalized hydrogels

HUVECs at a density of 1×10^5 cells were seeded into confocal dishes and allowed to adhere. The cells were then treated with extracts of PBS, GelMA, GelMA/ $\text{g-C}_3\text{N}_4$, GelMA/CAM, or GelMA/CAM@ $\text{g-C}_3\text{N}_4$ for 48 h. The extracts were aspirated, and the cells were fixed with 4 % para-formaldehyde for 30 min, permeabilized with 0.1 % Triton X-100 for 10

min, and washed three times with PBS. After blocking for 20 min, the cells were incubated with a primary CD31 antibody at 4 °C overnight, followed by a secondary antibody incubation at room temperature in the dark for 2 h. The cells were then stained with phalloidin for 30 min in the dark at room temperature and counterstained with DAPI for 10 min. Images were captured using a confocal microscope. The fluorescence intensity of CD31 was quantified using Image J software, with the experiment repeated three times.

2.14. Reactivation of RAW 264.7 macrophage function by functionalized hydrogels

RAW 264.7 cells at a density of 1×10^6 were seeded into confocal dishes and allowed to adhere. The cells were then treated with extracts of PBS, GelMA, GelMA/g-C₃N₄, GelMA/CAM, or GelMA/CAM@g-C₃N₄ for 24 h. The extracts were aspirated, and DCFH-DA working solution was added. After incubation at 37 °C in the dark for 30 min, the cells were stained with DAPI for 10 min. Images were taken using a confocal microscope, and ROS expression was quantified using Image J software. The experiment was repeated three times.

Similarly, RAW 264.7 cells at a density of 1×10^6 were seeded into confocal dishes and treated with extracts of PBS, GelMA, GelMA/g-C₃N₄, GelMA/CAM, or GelMA/CAM@g-C₃N₄ for 24 h. After the extracts were aspirated, the cells were fixed with 4 % paraformaldehyde for 30 min at room temperature, permeabilized with 0.1 % Triton X-100 for 10 min, and blocked for 20 min. The cells were then incubated with a rabbit anti-CD86 polyclonal antibody at 4 °C overnight, followed by incubation with a secondary antibody at room temperature in the dark for 2 h. Nuclei were stained with DAPI, and images were captured using a confocal microscope. CD86 fluorescence intensity was quantified using Image J software, with the experiment repeated three times.

2.15. qPCR analysis of RAW 264.7 inflammatory cytokine expression

RAW 264.7 cells at a density of 1×10^6 were seeded into a 6-well plate and treated with extracts of PBS, GelMA, GelMA/g-C₃N₄, GelMA/CAM, or GelMA/CAM@g-C₃N₄ for 24 h. Total RNA was extracted using a rapid RNA extraction kit, and the RNA concentration was determined. The RNA was reverse-transcribed into cDNA using a reverse transcription premix kit, and qPCR was performed using primers designed for the target genes (Table S 1). Gene expression was analyzed semi-quantitatively. The experiment was repeated three times.

2.16. Evaluation of antibacterial activity of functionalized hydrogels by spread plate method

The antibacterial activity of hydrogels was evaluated using the spread plate method. Briefly, 200 μ L of GelMA, GelMA/g-C₃N₄, GelMA/CAM, and GelMA/CAM@g-C₃N₄ hydrogels were prepared in 48-well plates. After complete gelation, 10 μ L of bacterial suspension (10^7 CFU mL⁻¹) was added to the surface of the hydrogels and incubated at 37 °C for 2 h under natural light. Subsequently, 1 mL of sterile PBS was added to each well to resuspend the bacteria. As a negative control, 10 μ L of bacterial suspension (10^7 CFU mL⁻¹) was added to 1 mL of PBS. Then, 100 μ L of the bacterial suspension was spread evenly onto agar plates, and incubated at 37 °C in a biochemical incubator for 20 h. The colonies were photographed and counted using Image J software, with each experiment repeated three times.

2.17. Evaluation of antibacterial activity of hydrogels by live/dead staining

The antibacterial activity of hydrogels was further assessed using a bacterial live/dead staining kit according to the manufacturer's instructions. SYTO 9 and PI were diluted in PBS (1:1000) and mixed with the bacterial suspension at room temperature for 20 min. The bacterial

suspension was then placed on a slide and observed under a confocal microscope, with images captured for further analysis. The experiments were repeated three times.

2.18. Observation of bacterial morphology

The bacterial morphology after treatment with different functionalized hydrogels was observed by scanning electron microscopy (SEM). Briefly, bacterial suspensions from different treatment groups were centrifuged at 4000 rpm for 10 min at 25 °C, and the bacterial pellet was collected. The bacteria were fixed in 2.5 % glutaraldehyde at 4 °C overnight. After centrifugation, the fixed samples were washed with PBS several times, followed by gradient dehydration using ethanol solutions at concentrations of 30 %, 50 %, 70 %, 85 %, 95 %, and 100 %, with each step lasting for 15 min. Finally, 20 μ L of the dehydrated bacterial sample was dropped onto a silicon wafer and air-dried. The samples were coated with gold and observed under SEM to examine bacterial morphology.

2.19. Evaluation of anti-biofilm activity of functionalized hydrogels by crystal violet staining

Bacterial suspensions (180 μ L/well) were seeded in a 96-well plate and incubated at 37 °C in a humidified environment for 24 h. After incubation, the planktonic bacteria were removed, and the wells were washed with PBS to remove loosely attached bacteria. PBS, GelMA, GelMA/g-C₃N₄, GelMA/CAM, and GelMA/CAM@g-C₃N₄ extracts were added to the wells, and the plates were incubated at 37 °C in a humidified environment for another 24 h. After incubation, the extracts and dead bacteria were washed away with PBS, and the remaining biofilm was fixed with 4 % formaldehyde for 15 min. The fixed biofilms were washed with PBS, and stained with 0.1 % crystal violet for 15 min at room temperature, and unbound dye was removed by washing with PBS. The plates were air-dried, and the crystal violet bound to the biofilm was solubilized using 33 % acetic acid. The absorbance was measured at 590 nm, with each experiment repeated three times.

2.20. Animals experiments

All animal experiments were reviewed and approved by the Animal Ethics Committee of North Sichuan Medical College (Approval No: 2024094) and conducted by national animal protection guidelines. All surgical procedures were performed under anesthesia, and all efforts were made to minimize pain, suffering, and death. A total of 100 healthy male SD rats (SPF grade, 8 weeks old, weighing 220–250 g) were anesthetized with sodium pentobarbital (20 mg/kg), and their backs were shaved. Full-thickness skin wounds (10 mm in diameter) were created on the rat backs using a circular punch and surgical scalpel. The rats (n = 3) were randomly divided into different groups. The wounds were infected with *Staphylococcus aureus* suspension (10^7 CFU/mL, 50 μ L) for 24 h to establish an infected wound model. The wounds were then treated with PBS, GelMA, GelMA/g-C₃N₄, GelMA/CAM, and GelMA/CAM@g-C₃N₄ hydrogels. On days 0, 3, 7, and 14, the infected wounds were photographed, and the healing process was observed. The wound area was measured using Image J software. Additionally, on day 3, the infected wound tissues and surrounding skin were excised, homogenized in 1 mL of sterile PBS, serially diluted, and plated on solid culture media for bacterial growth. The plates were incubated in a bacterial incubator for 12 h and photographed. During the wound healing process, skin tissue around the wound in each group was collected and fixed in 4 % paraformaldehyde. The tissue specimens were stained with hematoxylin-eosin (H&E), Masson's trichrome, Giemsa, and subjected to immunofluorescence staining for CD31, CD86, and CD206 (Chengdu Lilai Biotech Co., Ltd.). Additionally, to evaluate the in vivo toxicity of the hydrogel samples, visceral organs (heart, liver, spleen, lungs, kidneys) from the rats were collected for H&E staining. The experiments were repeated three times.

2.21. Statistical analysis

All data were statistically analyzed using SPSS 24.0 and GraphPad Prism 8 software. Independent sample t-tests were used to evaluate statistical differences between the two groups, while one-way ANOVA was employed for multiple-group comparisons. Data are presented as mean \pm standard deviation ($\bar{x} \pm s$). “ns” indicates no significant difference; * $p < 0.05$, ** $p < 0.01$, and *** $p < 0.001$ indicate statistically significant differences.

3. Results and discussion

3.1. Synthesis and characterization of g-C₃N₄

Fig. 1a showed the synthesis of g-C₃N₄ via a thermal polymerization method. Under TEM, g-C₃N₄ exhibited a layered sheet-like structure (Fig. 1b). XPS analysis confirmed that g-C₃N₄ consists of carbon (C) and nitrogen (N) elements (Fig. 1c). The XPS valence band spectrum indicated that g-C₃N₄ was composed of C-C, C=N-C, and N-C=N bonds (Fig. 1d and e). XRD results showed two characteristic peaks at 13.0° and 27.5°, confirming the successful synthesis of g-C₃N₄ (Fig. 1f) [38]. A

hydrogen peroxide assay kit was used to detect the production of ROS and a standard curve was established, showing that the amount of ROS produced by g-C₃N₄ was positively correlated with its concentration and light exposure time (Fig. 1g and Figure S 1).

3.2. Synthesis of copper alginate microspheres and construction of functionalized hydrogel system

Fig. 2a illustrated the schematic of the gas-cutting method used to synthesize copper alginate microspheres. Under a light microscope, the microspheres exhibit uniform round structures with a diameter of approximately $290.1 \pm 16.3 \mu\text{m}$ (Fig. 2b and c). Fig. 2d showed that different hydrogels formed a gel state after 30 s of UV light exposure. SEM analysis revealed a smooth surface for GelMA hydrogels, which became rough after incorporating g-C₃N₄. In the G-C-g group, microspheres were attached to the surface, and element mapping showed that the gel surface was composed of C, N, O, and Cu, confirming the successful construction of the hydrogel-microsphere system (Fig. 2e and f). The swelling curves of the hydrogels in different systems were similar, with no significant change in swelling properties after the incorporation of g-C₃N₄ and CAM. The hydrogels demonstrated excellent adhesion

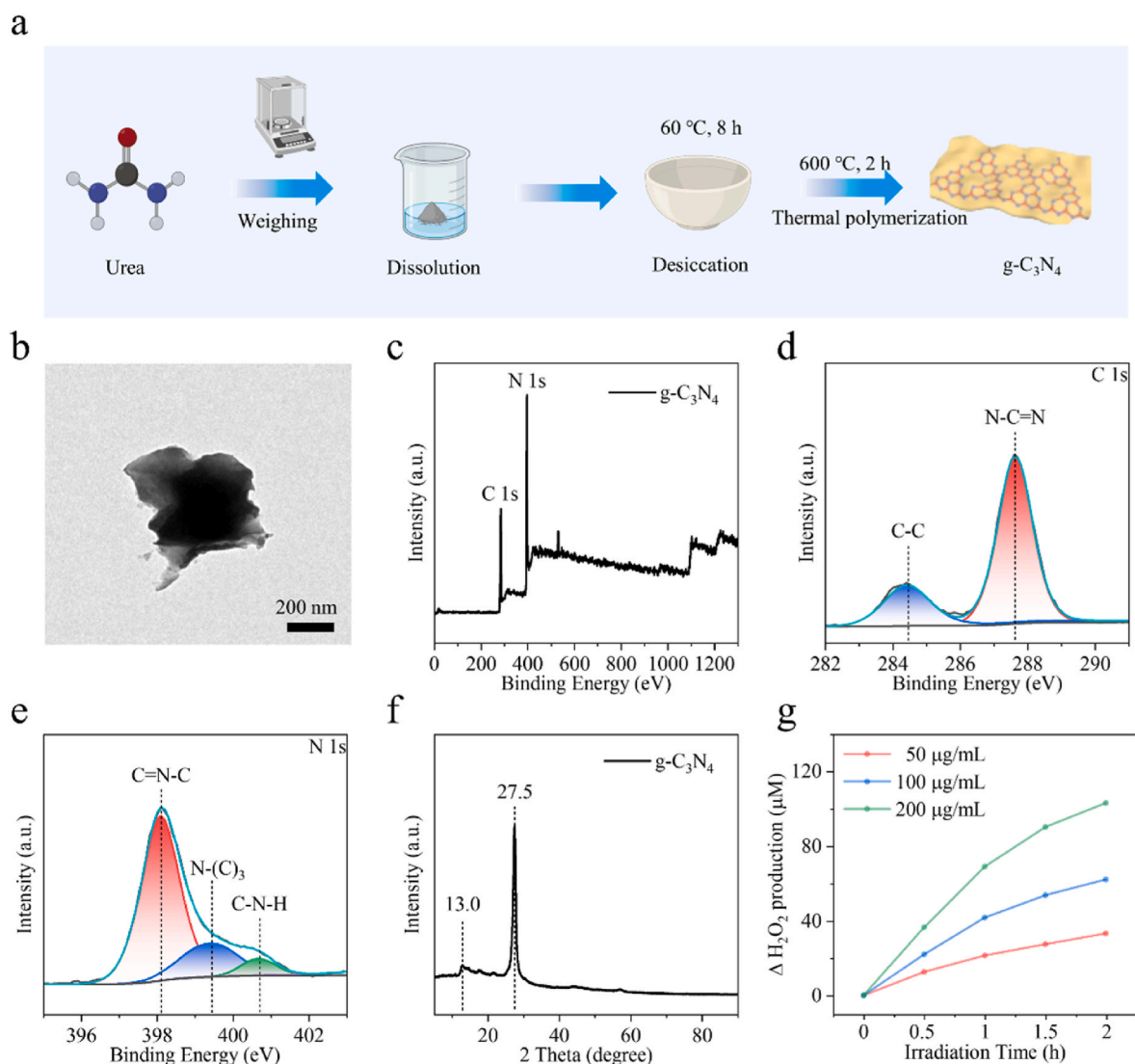


Fig. 1. Synthesis and characterization of g-C₃N₄. (a) Schematic illustration of g-C₃N₄ synthesis. (b) Morphology of g-C₃N₄ under transmission electron microscopy (TEM). (c) XPS spectrum of g-C₃N₄. (d) Valence band spectrum of C 1s in g-C₃N₄. (e) Valence band spectrum of N 1s in g-C₃N₄. (f) XRD pattern of g-C₃N₄. (g) H₂O₂ production by g-C₃N₄ at different concentrations and time points.

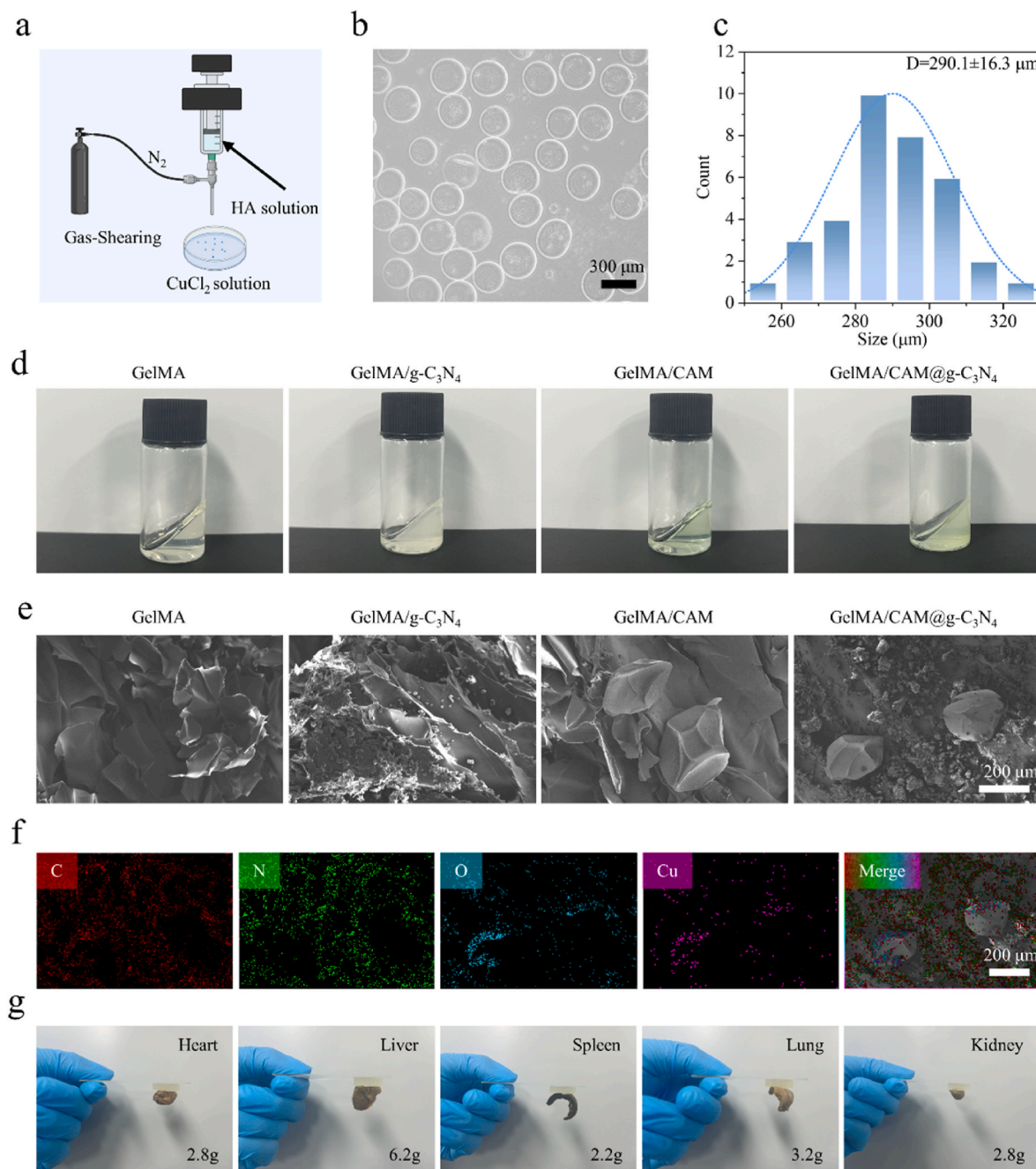


Fig. 2. Synthesis of copper alginate microspheres and characterization of the functionalized hydrogel system. (a) Schematic illustration of copper alginate microsphere synthesis via the air-cutting method. (b) Image of copper alginate microspheres under a light microscope. (c) Microsphere size distribution under a light microscope. (d) Images of different functionalized hydrogel systems post-gelation. (e) Microstructure of different functionalized hydrogels under a scanning electron microscope (SEM). (f) Elemental mapping of GelMA/CAM@g-C₃N₄ hydrogel. (g) Adhesion test of GelMA/CAM@g-C₃N₄ hydrogel.

to the heart, liver, spleen, lungs, and kidneys (Fig. 2g). The swelling and rheological properties of GelMA hydrogel did not change significantly after loading g-C₃N₄ and CAM step by step (Fig. S 2-S 3). Using a copper ion assay kit, a standard curve for copper ions was established, and the UV spectra of different concentrations of g-C₃N₄ were measured to create a standard curve. The release curves of functionalized hydrogel microspheres showed rapid release of g-C₃N₄ and copper ions within 0–12 h, followed by sustained release (Fig. S 4-S 7).

3.3. Biocompatibility, scratch, and tube formation assays of functionalized hydrogel microspheres

The CCK-8 assay showed that g-C₃N₄ concentrations exceeding 150 μg/mL significantly affect RAW264.7 cell viability, and copper ion concentrations exceeding 40 μg/mL notably reduce HUVEC cell viability. Therefore, a concentration of 150 μg/mL for g-C₃N₄ and 40 μg/mL for copper ions was selected for subsequent experiments (Fig. S 8-S 11). Live-dead cell staining with extracts from different hydrogel groups showed that the functionalized hydrogel microspheres exhibited excellent biocompatibility with RAW264.7 and HUVECs (Fig. 3a and Fig. S 12-S 14).

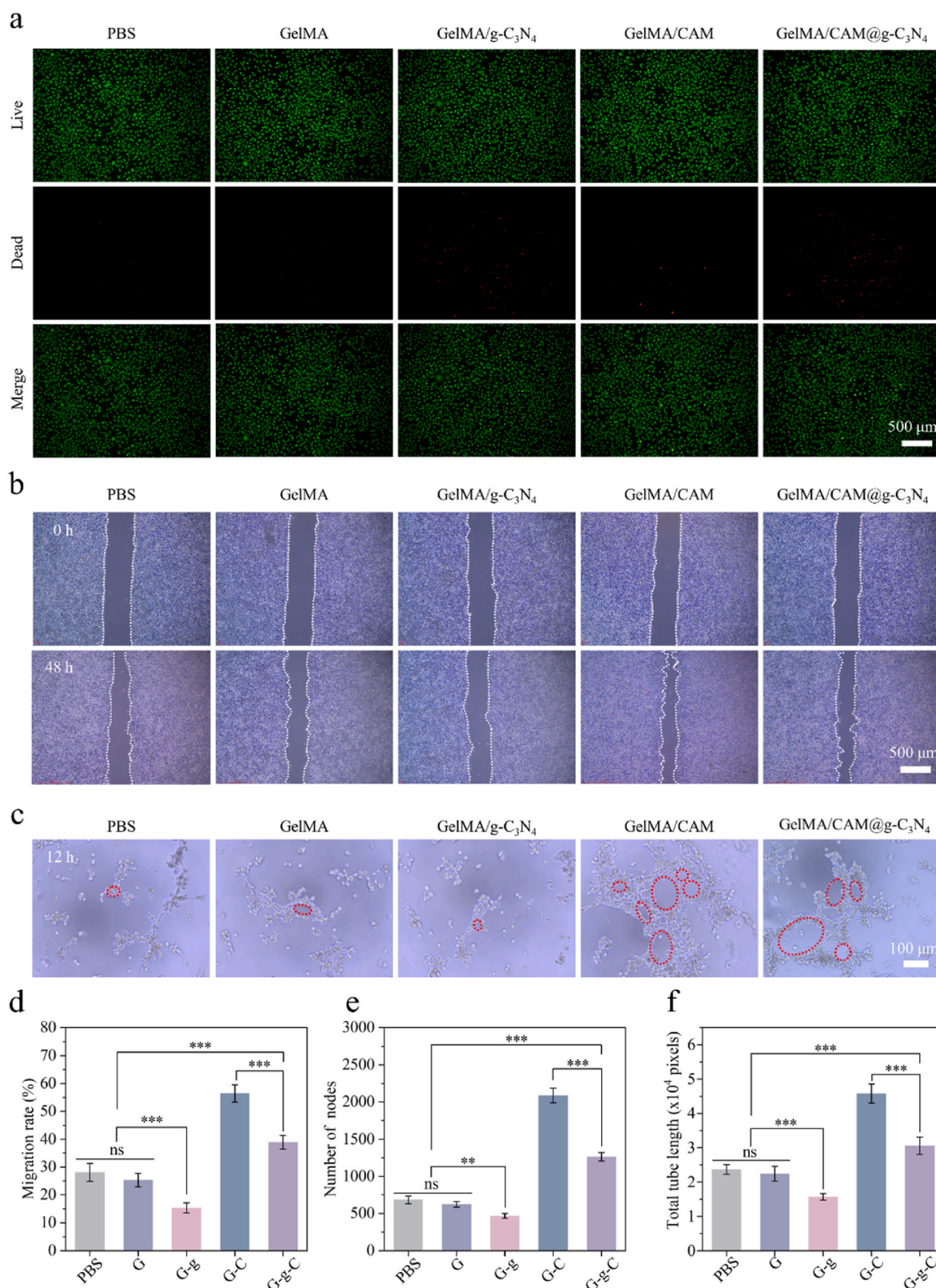


Fig. 3. Biocompatibility, Cell migration assay, and tube formation assay of the functionalized hydrogel microspheres. (a) Live/dead staining of different functionalized hydrogel systems. (b) Cell migration assay. (c) Tube formation assay. (d) Quantitative analysis of cell migration assays. (e) Quantitative analysis of tube formation nodes. (f) Quantitative analysis of tube formation tube length. G represents GelMA; G-g represents GelMA/g-C₃N₄; G-C represents GelMA/CAM; G-g-C represents GelMA/CAM@g-C₃N₄.

Scratch assay results showed that the G-g group extract slowed cell migration, while the G-C-g group significantly accelerated cell migration compared to the PBS group (Fig. 3b and d). Tube formation assays revealed that the G-g group extract reduced tube formation and total length in HUVECs, while the G-C-g group significantly promoted tube formation and total length compared to the PBS group (Fig. 3c–e, and f). After 24 h of intervention with different hydrogel systems on HUVECs, the G-C-g group significantly promoted CD31 expression compared to the PBS group (Fig. S 15 and S 16).

3.4. Functionalized hydrogel microspheres re-roused macrophage M1 function

After treating M0 macrophages with extracts from different systems, the DCFH-DA probe results showed that both the G-g and G-C-g groups induced macrophages to exhibit a pro-inflammatory phenotype, with significantly higher ROS expression than the PBS group (Fig. 4a and Fig. S 17). CD86 immunofluorescence analysis showed that the G-g and G-C-g groups had higher fluorescence intensity than the PBS group (Fig. 4b and Fig. S 18). Further RNA extraction and PCR results indicated that the expression of pro-inflammatory factors (IL-1, IL-6, TNF- α) significantly increased in the G-g and G-C-g groups compared to the PBS group (Fig. S 19).

3.5. Antibiofilm activity and mechanism of functionalized hydrogel microspheres in vitro

In infected environments, bacteria protect themselves from immune system attacks and exogenous bactericides by secreting EPS (extracellular polymeric substances) to form biofilms, which contribute to the persistence and resistance of biofilm-related infections. In this study, bacteria were seeded on the hydrogel surface, plated on agar, and observed through photographs and quantitative Image J analysis. Plate coating results indicated that a large number of colonies grew on the surfaces in the PBS and G groups. However, after intervention with the G-g and G-C groups, *Staphylococcus aureus* growth was inhibited, with the G-C-g group showing a significant reduction in bacterial colonies (Fig. 5a and Fig. S 20). Bacterial live-dead staining revealed a marked increase in dead bacteria in the G-C-g group compared to the PBS group (Fig. 5b). SEM analysis showed intact bacterial cell walls in the PBS and G groups, while the G-C-g group displayed disrupted bacterial walls and cytoplasmic leakage (Fig. 5c). Similar results were obtained when the system was tested on *Escherichia coli*, where the G-C-g group exhibited significant inhibitory effects on bacterial growth compared to the PBS group (Fig. 5d and Fig. S 21). Live-dead bacterial staining further confirmed that the G-C-g group had a higher proportion of dead bacteria compared to the PBS group (Fig. 5e). SEM observations revealed disrupted *E. coli* cell walls in the G-C-g group compared to the PBS group (Fig. 5f). Using crystal violet staining, hydrogels from different groups demonstrated that the G-C-g group exhibited significant inhibitory effects on both *S. aureus* and *E. coli* compared to the PBS group (Fig. S 22 and S 23).

Further, after intervening with PBS and the G-C-g group on *S. aureus*, bacterial gene sequencing revealed similar gene distribution patterns between the G-C-g and PBS groups, which can be used for subsequent experimental validation (Fig. 6a). Compared to the PBS group, the G-C-g group exhibited upregulation of 302 metabolites and downregulation of 349 metabolites (Fig. 6b). A clustering heat map illustrated the consistency of metabolite changes after treatment, highlighting differences in metabolite expression between the two groups (Fig. 6c). KEGG enrichment analysis indicated that the functionalized hydrogel microspheres downregulated glycolysis, oxidative phosphorylation, the phosphotransferase system, amino acid metabolism (alanine, aspartate, and glutamate metabolism), purine, and pyrimidine metabolism (Fig. 6d). GO enrichment analysis revealed that the system inhibited processes such as carbohydrate derivative biosynthesis, lipoteichoic acid

metabolism, and lipoteichoic acid biosynthesis (Fig. 6e). Fig. 6f illustrated the antibacterial mechanism of the functionalized hydrogel microspheres. The diagram showed that the ROS generated by g-C₃N₄ disrupts the biofilm, followed by the release of copper ions from copper alginate microspheres, which blocked bacterial ABC transporters, leading to impaired nutrient exchange. Copper ions overload within the bacteria first induced downregulation of glycolysis and oxidative phosphorylation, resulting in reduced energy metabolism. This was followed by downregulation of purine and pyrimidine metabolism, impairing DNA replication and repair systems. Additionally, triglyceride metabolism was downregulated, and copper ions induced lipid peroxidation, ultimately leading to bacterium-like copper-induced cell death.

3.6. Functionalized hydrogel microspheres promote biofilm-associated wound healing in vivo

Fig. 7a illustrated the schematic diagram of biofilm-associated chronic wound healing and the application of functionalized hydrogel microspheres on the wound site. A circular wound model with a 10 mm diameter was created on the backs of SD rats, followed by inoculation with *S. aureus*. When the wound exhibited purulent exudation, successful model establishment was confirmed. Subsequently, hydrogels from different groups were applied to the wounds, and healing progress was documented. Gross images of wound healing demonstrated that interventions with the g-C₃N₄ and CAM groups accelerated wound healing, while the G-C-g group, through the synergistic effects of g-C₃N₄ and CAM, significantly accelerated wound healing compared to the PBS group (Fig. 7b–d). On day 3 of wound healing, wound exudates were collected for plate analysis, revealing a reduction in bacterial numbers in the g-C₃N₄ and CAM groups, with the G-C-g group exhibiting the most significant reduction compared to the PBS group (Fig. 7e and Fig. S 24). On day 3, Giemsa staining of wound tissues showed large aggregations of *S. aureus* in the PBS and G groups, whereas bacterial numbers were reduced in the G-g and G-C groups. The G-C-g group showed only a few residual bacteria, significantly fewer than in other groups (Fig. 7f). H&E staining on day 7 demonstrated partial wound contraction in the G-g and G-C groups, while the G-C-g group showed significant wound contraction, leaving the shortest wound length compared to the PBS group (Fig. 8a and c). By day 14, wound healing had further progressed in all groups, with the G-C-g group displaying the shortest wound diameter (Fig. 8a). Masson's staining on day 7 revealed higher collagen deposition in the G-g and G-C groups compared to the PBS group, while the G-C-g group showed the highest collagen deposition with statistical significance (Fig. 8b and d). By day 14, collagen deposition had further increased in all groups, with the G-C-g group exhibiting the highest collagen deposition (Fig. 8b). Immunofluorescence staining of wound tissues on day 3 revealed lower CD86 and CD206 expression in the PBS and G groups, whereas CD86 expression significantly increased in the G-g and G-C-g groups compared to the PBS group (Fig. 9a and Figure S 25). On day 7, immunofluorescence results showed increased CD206 expression in the G-g and G-C groups, with the G-C-g group exhibiting significantly higher CD206 expression compared to the other groups (Fig. 9b and Figure S 26). Additionally, CD31 immunofluorescence staining of wound tissues showed significantly higher CD31 expression in the G-C-g group compared to the other groups, indicating that the wound healing had progressed to the proliferation phase (Fig. S 27 and S 28). On day 14 of wound healing, H&E staining of the heart, liver, kidneys, lungs, and spleen of SD rats showed no significant signs of inflammation, necrosis, or other pathological changes (Fig. S 29).

4. Discussion

Bacterial infectious diseases are an increasing public health challenge [39,40]. The formation of biofilms and the immune evasion they induce in macrophages both hinder the wound healing process. Therefore, disrupting bacterial biofilms and re-rousing macrophage M1

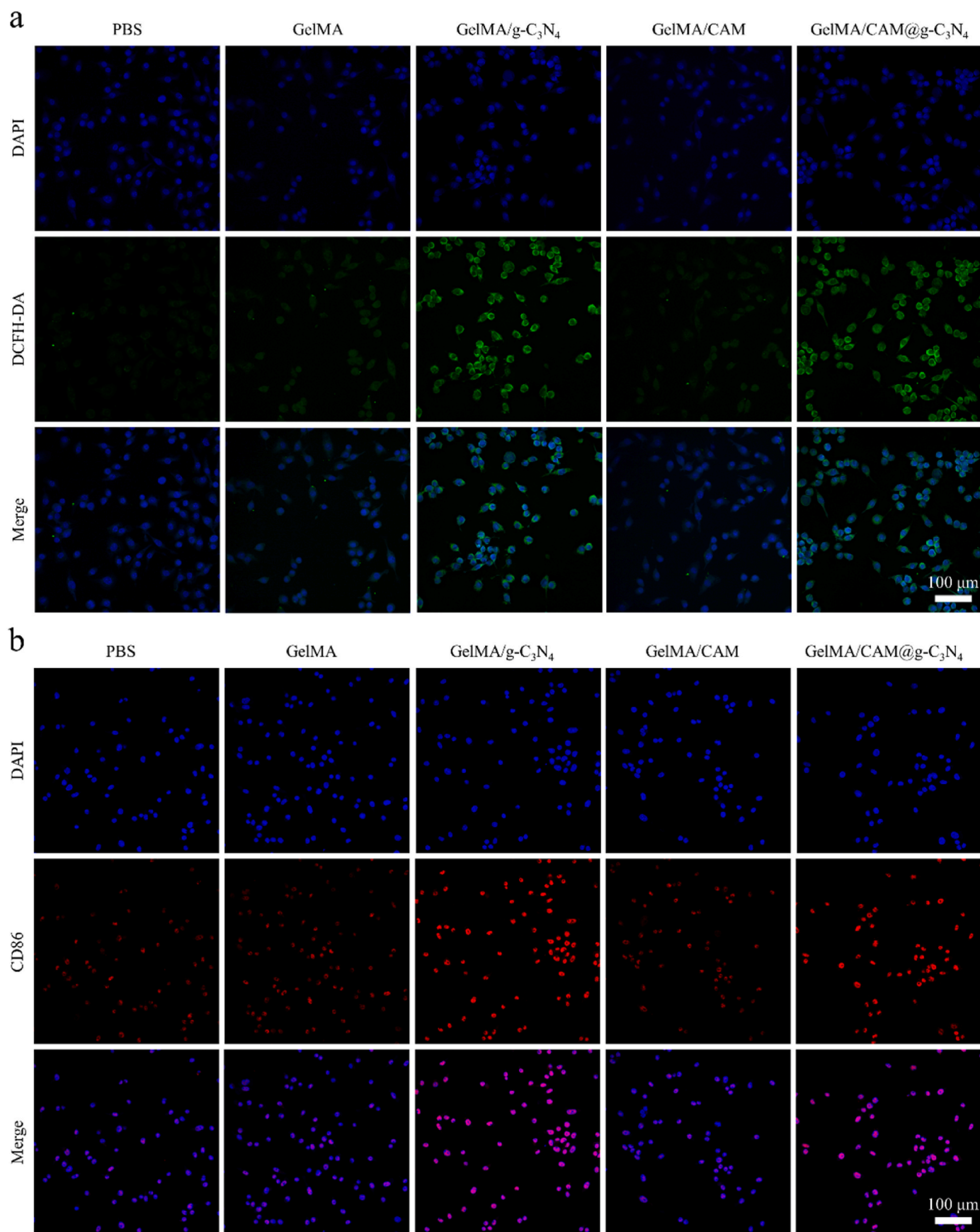


Fig. 4. Functionalized hydrogel microspheres Re-rousing macrophage M1 function. (a) ROS probe for different functionalized hydrogel systems. (b) CD86 immunofluorescence of different functionalized hydrogel systems.

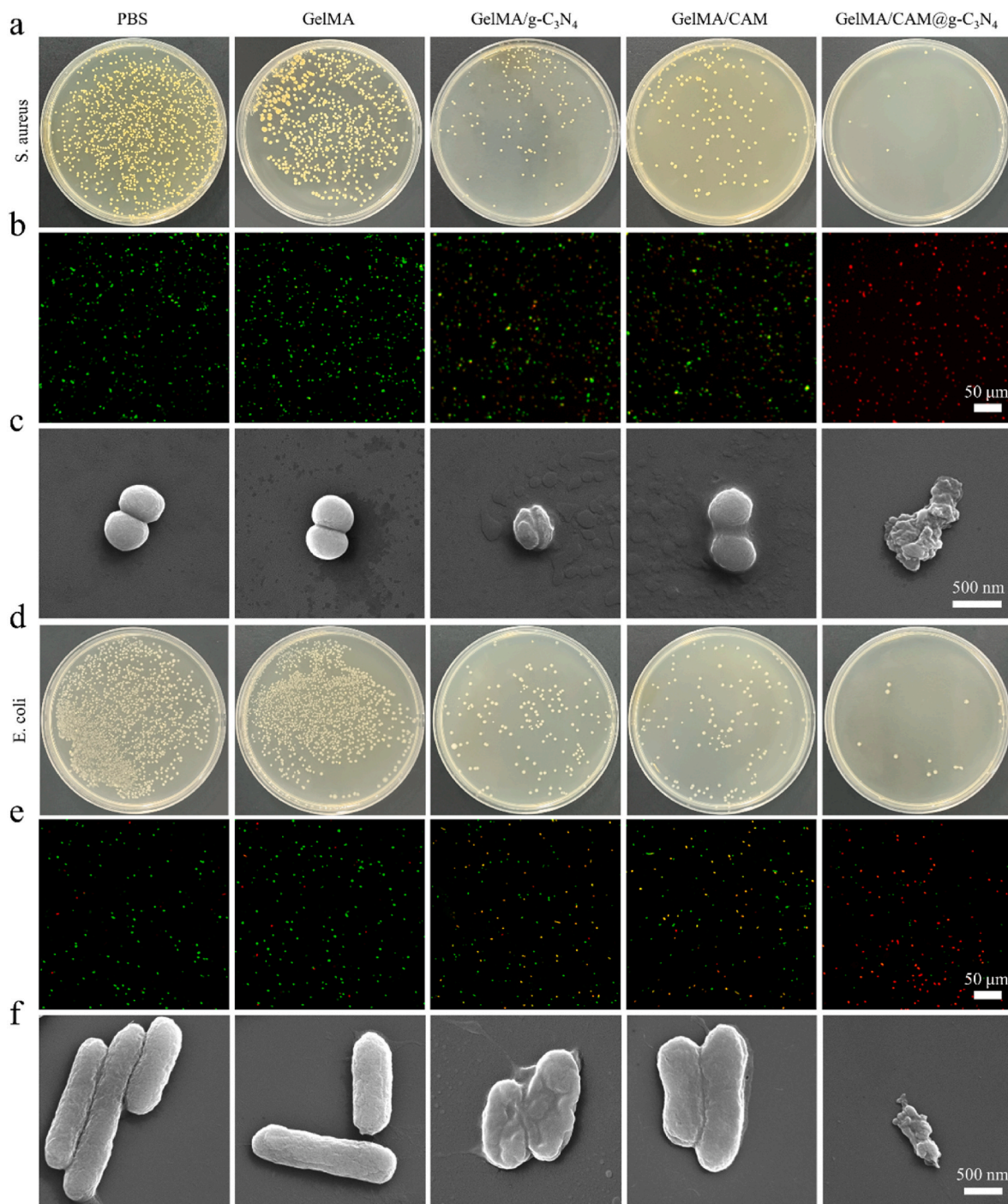


Fig. 5. Functionalized hydrogel microspheres exhibiting antibacterial effects in vitro. (a) Plate streaking of *Staphylococcus aureus* after intervention with different functionalized hydrogels. (b) Live/dead staining. (c) SEM imaging. (d) Plate streaking of *Escherichia coli* after intervention with different functionalized hydrogels. (e) Live/dead staining. (f) SEM imaging.

functionality are key strategies for promoting chronic wound regeneration. In this study, we developed a chronic wound repair system by synthesizing g-C₃N₄ through thermal polymerization and CAM using gas-cutting methods. Further, we encapsulated g-C₃N₄ and CAM into GelMA to construct a system capable of disrupting biofilms and reawakening macrophage M1 function.

In recent years, with the rapid development of nanotechnology, the application of nanomaterials in the field of antibacterial therapy has achieved significant success. The g-C₃N₄ is a novel inorganic non-metallic photoactive material with a two-dimensional layered aromatic polycyclic structure composed of sp²-hybridized C and N atoms,

and its C-N bond length is uniform [41,42]. In this study, g-C₃N₄ was successfully synthesized via thermal polymerization and characterized by TEM, XRD, and XPS analyses, including its valence band spectrum. Using an H₂O₂ assay kit under light exposure, we demonstrated that g-C₃N₄ exhibits peroxidase (POD) activity.

Microsphere structures can effectively encapsulate active ingredients, achieving protection and sustained release [43]. Sodium alginate exchanges its Na⁺ with divalent cations such as Ca²⁺, Cu²⁺, and Ba²⁺, forming a stable biopolymer with a unique three-dimensional structure [44]. In our constructed system, copper alginate microspheres were successfully synthesized via gas-cutting methods, and

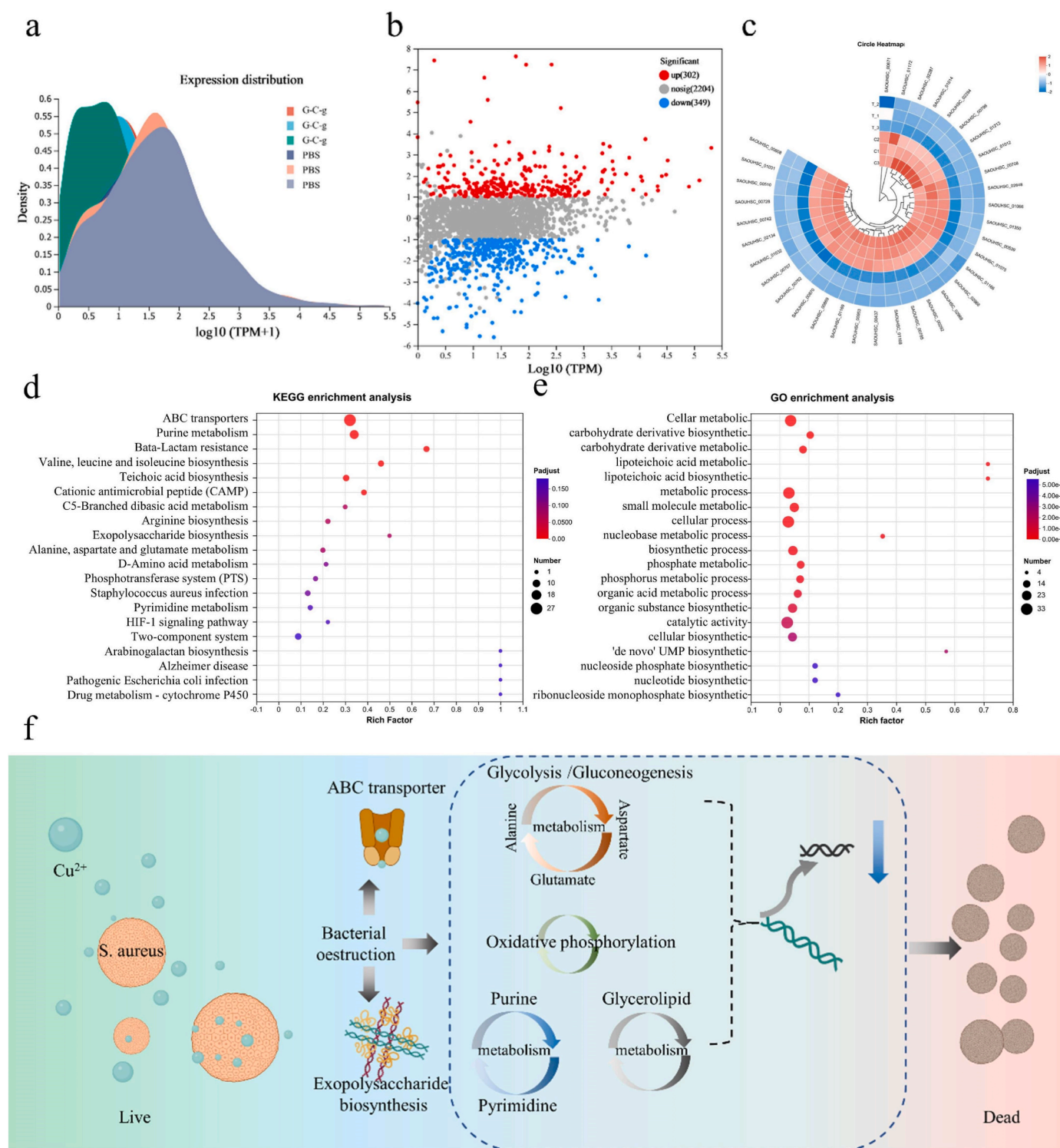


Fig. 6. Antibacterial mechanism analysis of functionalized hydrogel microspheres. (a) Gene expression distribution across different treatment groups. (b) MA plot of gene expression in different treatment groups. (c) Clustering heatmap of different treatment groups. (d) KEGG analysis. (e) GO analysis. (f) Schematic illustration of copper-like bacterial death induced by *Staphylococcus aureus*. G represents GelMA; G-g represents GelMA/g-C₃N₄; G-C represents GelMA/CAM; G-C-g represents GelMA/CAM@g-C₃N₄.

uniform spherical structures were observed under a light microscope, showing sustained release of Cu²⁺ during degradation. Hydrogels are one of the most important biomaterials, attracting attention for medical applications such as wound healing, tissue engineering, and drug delivery [45]. SEM analysis revealed a uniform porous three-dimensional network structure, with microspheres and g-C₃N₄ attached to the

surface, confirming the successful construction of the functionalized hydrogel microsphere wound healing system. The RGD sequence in GelMA hydrogels promoted adhesion between the hydrogel and cells. Additionally, the water molecules in the hydrogel could form hydrogen bonds with water molecules on the wound surface, enhancing the contact between the hydrogel and the wound [46]. Furthermore, water

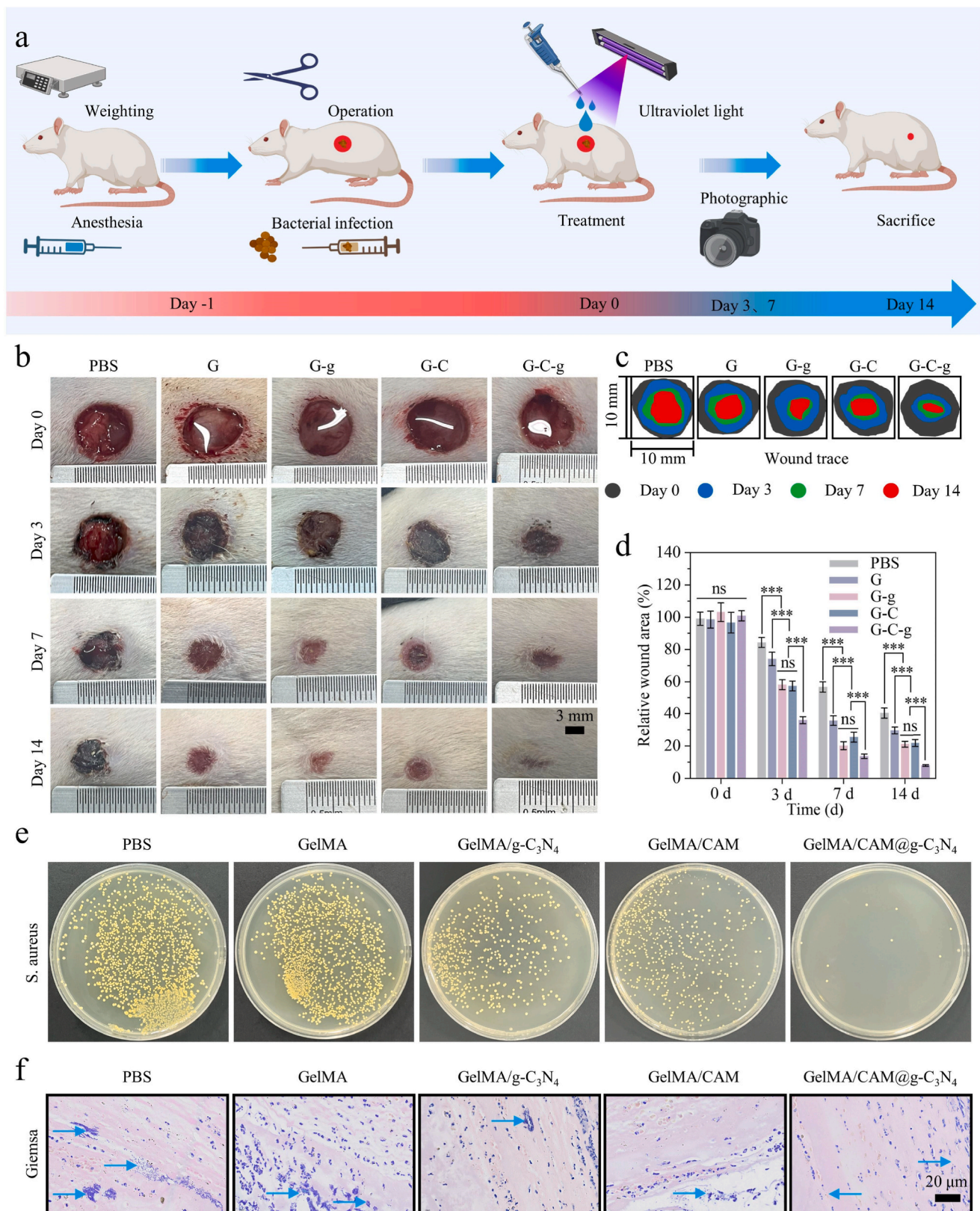


Fig. 7. Functionalized hydrogel microspheres promoting biofilm wound healing in vivo. (a) Schematic illustration of biofilm model establishment and treatment of biofilm wounds with functionalized hydrogels. (b) Representative images of biofilm wounds treated with different functionalized hydrogels. (c) Tracked images of biofilm wound healing. (d) Quantitative analysis of remaining wound area during healing. (e) Plate streaking of wound exudates on day 3 post-treatment. (f) Giemsa staining of different functionalized hydrogels. G represents GelMA; G-g represents GelMA/g- C_3N_4 ; G-C represents GelMA/CAM; G-C-g represents GelMA/CAM@g- C_3N_4 .

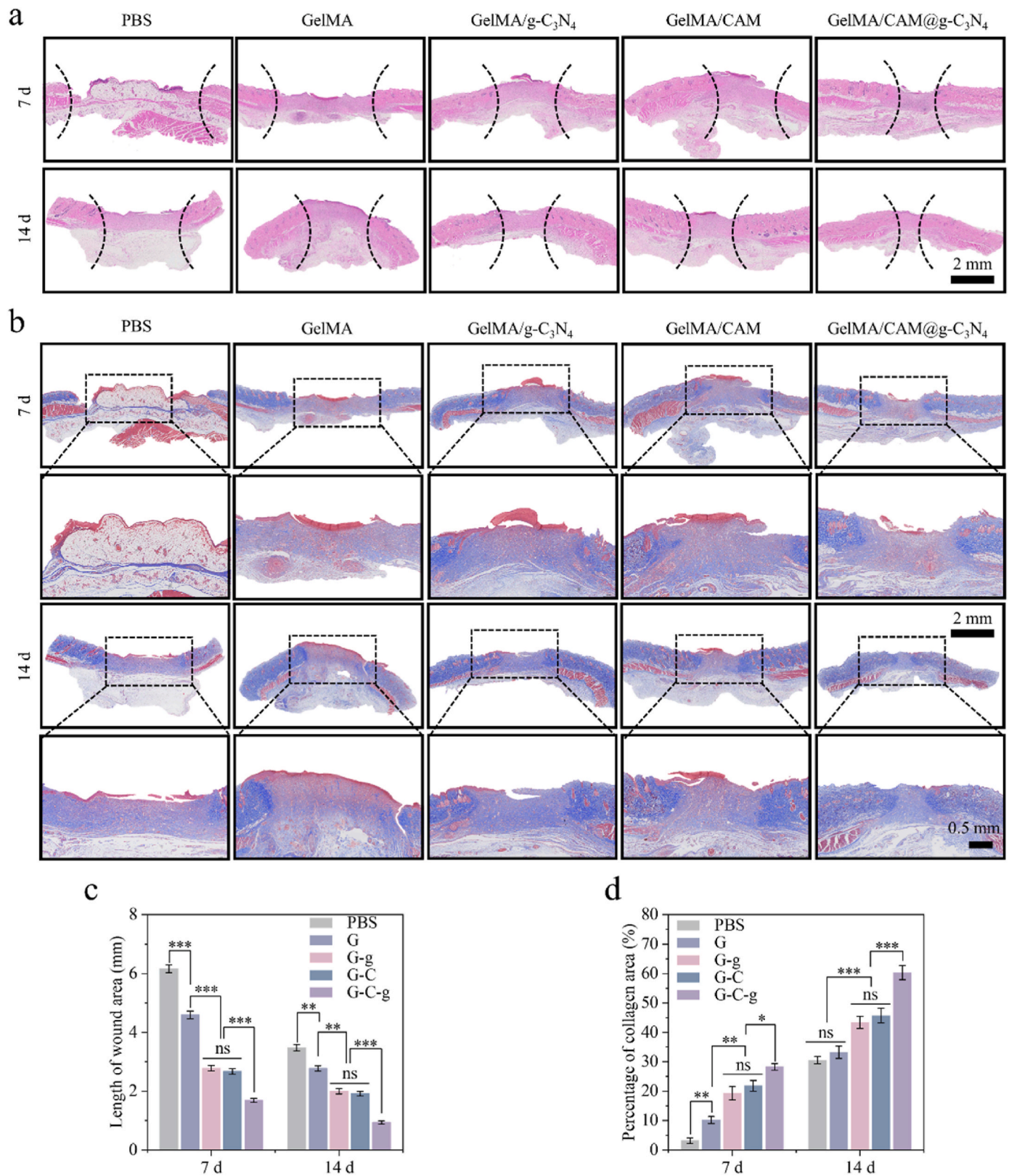


Fig. 8. Functionalized hydrogel microspheres promoting biofilm wound healing. (a) H&E staining after treatment with different functionalized hydrogels. (b) Masson staining after treatment with different functionalized hydrogels. (c) Quantitative analysis of wound length after intervention with different functionalized hydrogels. (d) Quantitative analysis of collagen deposition rate after intervention with different functionalized hydrogels. G represents GelMA; G-g represents GelMA/g-C₃N₄; G-C represents GelMA/CAM; G-C-g represents GelMA/CAM@g-C₃N₄.

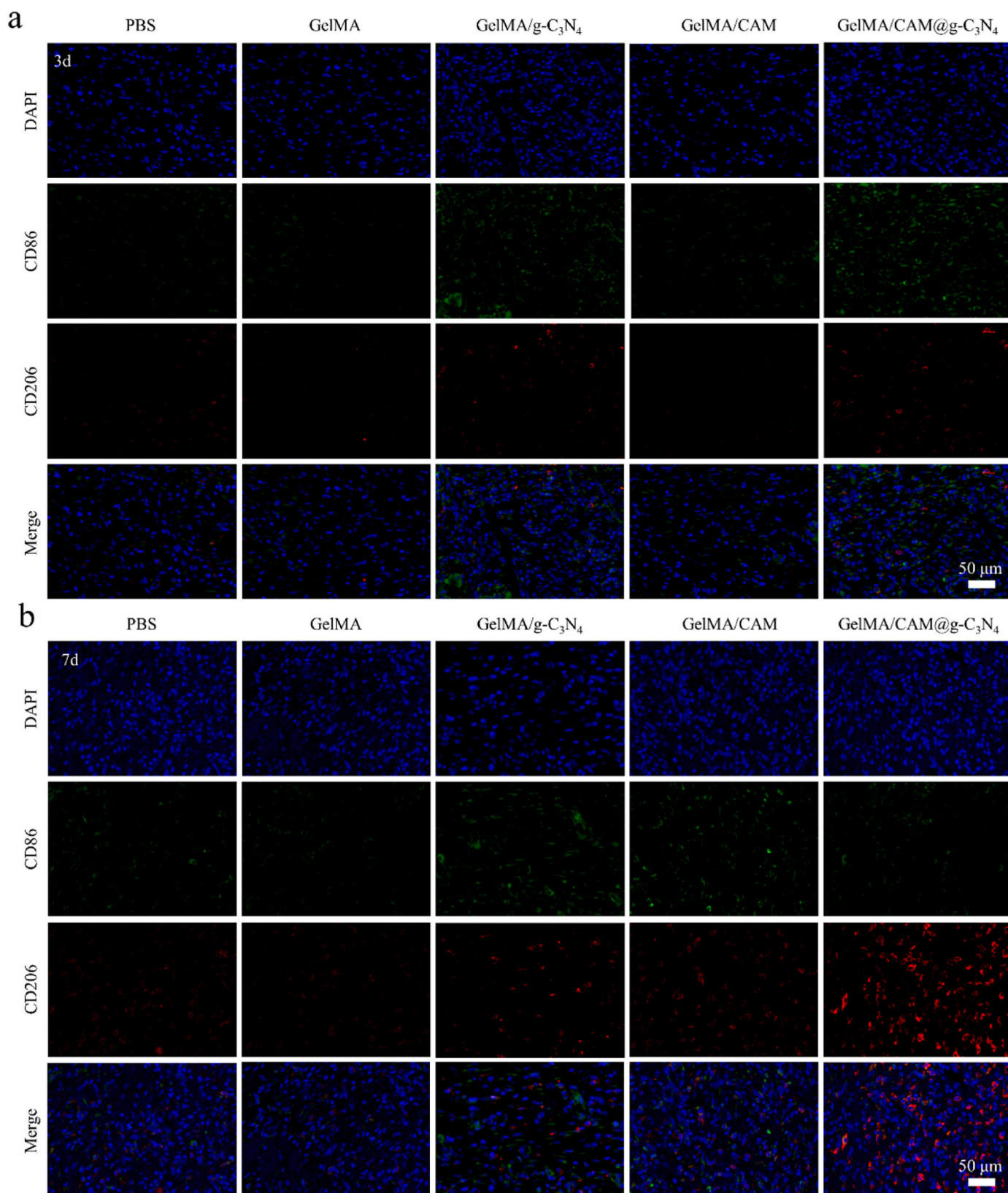


Fig. 9. Functionalized hydrogel microspheres promoting biofilm wound healing in vivo. (a) Representative images of CD86 and CD206 immunofluorescence on day 3 post-treatment with different functionalized hydrogels. (b) Representative images of CD86 and CD206 immunofluorescence on day 7 post-treatment with different functionalized hydrogels.

molecules penetrated the wound tissue via physical osmosis, forming a water layer that further consolidates the connection between the hydrogel and the wound. These adhesion mechanisms played a critical role in tissue repair and regeneration.

Biocompatibility aims to assess the toxicity and safety of biomaterials in cells, ensuring that therapeutic effects are achieved while minimizing potential side effects. In this study, the CCK-8 assay results indicated that when the g-C₃N₄ concentration did not exceed 150 µg/mL and Cu²⁺ concentration did not exceed 40 µg/mL, there was no significant toxicity to the cells. However, higher concentrations of nanomaterials and metal ions may cause toxicity through various mechanisms, such as disrupting the cell membrane, inducing oxidative stress, triggering intracellular metabolic disorders, and causing ionic homeostasis imbalance. Based on CCK-8 and live-dead staining assays, the functionalized hydrogel microspheres demonstrated excellent biocompatibility.

Macrophages possess high plasticity and are polarized into “classically activated” pro-inflammatory M1 and “alternatively activated” anti-inflammatory M2 phenotypes during different phases of wound healing [47]. In this study, g-C₃N₄ successfully mimicked POD enzyme activity and generated ROS. Through ROS probing, CD86 immunofluorescence, and PCR assays, the results showed that g-C₃N₄ could promote macrophage ROS production and upregulate the expression of CD86, IL-1, IL-6, and TNF-α pro-inflammatory cytokines, successfully re-rousing macrophage M1 pro-inflammatory function. ROS, as a driving signal for M1 macrophage polarization, initiates cell cycle and metabolic reprogramming through pathways such as ATM-CHK2, NF-κB, and MAPK, regulating macrophage M1 phenotype polarization, inducing the expression of inflammatory cytokines, and enhancing their phagocytic function [47–49]. Microbial aggregation at wound sites and the development of resistance to available antibiotics are major concerns [50]. To survive under harsh conditions, including exposure to known antibiotics, microorganisms form biofilms a unique structure whose formation involves quorum sensing, environmental stress, nutrient availability, hydrodynamic conditions, intercellular communication, signaling cascades, and secondary messengers. Alternative therapies that disrupt bacterial structure and function by generating ROS and binding metal ions have gained considerable attention in recent years [51].

Neovascularization supplies wounds with sufficient blood and oxygen to support cell survival and tissue regeneration [52]. In chronic wounds, insufficient blood perfusion exacerbates infection symptoms associated with microbes and often complicates the healing process [53]. In this study, the migration assay, tube formation assay, and CD31 immunofluorescence analysis results indicated that the functionalized hydrogel microspheres could promote endothelial cell migration, tube formation, and CD31 expression. Current research suggests that Cu²⁺ can activate signaling pathways such as Wnt, PI3K/Akt, MAPK, and hypoxia-inducible factor 1α (HIF-1α), upregulating the expression of angiogenic factors, including vascular endothelial growth factor (VEGF), platelet-derived growth factor (PDGF), and HIF-1α, thereby inducing angiogenesis [49,54]. Using a chronic wound infection model with *S. aureus*, our system re-rousing macrophage M1 function by day 3, clearing pathogens and cellular debris, and shifting the chronic wound microenvironment towards an inflammatory phase. By day 7, macrophages had transitioned to the M2 phenotype, further promoting CD31 expression and collagen deposition, enabling the transition from the inflammatory phase to the proliferative remodeling phase, thereby greatly enhancing chronic wound healing efficiency.

In summary, based on the pathological conditions of biofilm formation and macrophage immune evasion in wound sites, the functionalized hydrogel microspheres developed in this study effectively disrupted bacterial biofilms and reawakened pro-inflammatory macrophage function, thereby transforming the microenvironment of chronically infected wounds into one conducive to physiological healing, ultimately promoting wound healing.

5. Conclusion

This study addresses the critical mechanisms of biofilm formation and macrophage immune evasion, which lead to impaired wound healing, by constructing a functionalized hydrogel microsphere wound repair system (GelMA/CAM@g-C₃N₄) with antibiofilm properties and the ability to re-rousing macrophage M1 function. This system effectively disrupted bacterial biofilms by generating ROS and re-roused macrophage M1 function. Additionally, the release of Cu²⁺ interfered with bacterial energy metabolism, biosynthesis, and lipid metabolism processes, leading to copper-like bacterial cell death. Furthermore, this system promoted CD31 expression in endothelial cells, effectively transforming the pathological microenvironment of chronic wounds into one that facilitated regeneration. This innovative approach provides a promising solution for the treatment of chronic wounds.

CRedit authorship contribution statement

Chao Xiang: Writing – original draft, Visualization, Validation, Methodology, Investigation, Funding acquisition, Formal analysis, Data curation, Conceptualization. **Chaoyu Pu:** Writing – original draft, Visualization, Validation, Methodology, Investigation, Formal analysis, Data curation. **XueMei Zhong:** Writing – original draft, Visualization, Formal analysis, Data curation. **Yong Wang:** Validation, Project administration, Data curation. **Weiyong Song:** Validation, Resources, Project administration, Data curation. **Xingkuan Wang:** Validation, Project administration, Funding acquisition. **Kemiao Chen:** Validation, Project administration. **Kai Li:** Validation, Resources, Project administration. **Yue Luo:** Validation, Resources, Project administration, Funding acquisition. **Ke Jiang:** Resources, Funding acquisition, Conceptualization. **Dianming Jiang:** Writing – review & editing, Project administration, Methodology, Investigation.

Ethics approval and consent to participate

All animal experiments in this study were approved by the Ethics Committee of the Animal Experimentation Centre of North Sichuan Medical College (approval number: 2024094).

Funding

This work was supported by Doctoral Research Launch Fund Project of North Sichuan Medical College Affiliated Hospital (CBY23-QDA23), Research Project of Sichuan Provincial Department of Science and Technology (2025ZNSFSC1789), Health Commission of Sichuan Province Medical Science and Technology Program (24QNMP096), Research Project Nanchong Science and Technology Bureau (23JCYJPT0036), Special Project for the Central Government to Guide the Development of Local Science and Technology in Sichuan Province (2024ZYD0190), Research Project of the Affiliated Hospital of North Sichuan Medical College (2024GC011, 2024MPZK013 and 2024MPZK015).

Declaration of competing interest

We confirm that the manuscript has been read and approved by all authors and that there is no other person who satisfies the criteria for authorship but is not listed. We also confirm that all authors have approved the order of authorship listed in the manuscript. The manuscript has not been previously published in any language anywhere, and it is not under consideration for publication by another journal.

Acknowledgments

We would also like to acknowledge BioRender, which was used to create a Schematic diagram in this article. We also wish to express our deep appreciation to the North Sichuan Medical College Innovation

Center for Science and Technology for providing the experimental platform that was crucial for our research. At the same time, we thank Majorbio for providing the genetic testing platform.

Appendix A. Supplementary data

Supplementary data to this article can be found online at <https://doi.org/10.1016/j.mtbio.2025.101571>.

Data availability

Data will be made available on request.

References

- [1] V. Falanga, R.R. Isseroff, A.M. Soulika, et al., Chronic wounds, *Nat. Rev. Dis. Primers* 8 (1) (2022) 50.
- [2] M. Falcone, B. De Angelis, F. Pea, et al., Challenges in the management of chronic wound infections, *J. Glob. Antimicrob. Resist.* 26 (2021) 140–147.
- [3] Y. Liu, L. Shi, L. Su, et al., Nanotechnology-based antimicrobials and delivery systems for biofilm-infection control, *Chem. Soc. Rev.* 48 (2) (2019) 428–446.
- [4] N.A. Kungwani, J. Panda, A.K. Mishra, et al., Combating bacterial biofilms and related drug resistance: role of phyto-derived adjuvant and nanomaterials, *Microb. Pathog.* 195 (2024) 106874.
- [5] Q. Xu, Y. Hua, Y. Zhang, et al., A biofilm microenvironment-activated single-Atom iron nanozyme with NIR-controllable nanocatalytic activities for synergetic bacteria-infected wound therapy, *Adv. Healthcare Mater.* 10 (22) (2021) e2101374.
- [6] Y. Wang, F. Wu, Y. Li, et al., Ellagic acid-modified gold nanoparticles to combat multi-drug resistant bacterial infections in vitro and in vivo, *Mater. Horiz.* (2024) null.
- [7] R. Funari, A.Q. Shen, Detection and characterization of bacterial biofilms and biofilm-based sensors, *ACS Sens.* 7 (2) (2022) 347–357.
- [8] J. Mei, D. Xu, L. Wang, et al., Biofilm microenvironment-responsive self-assembly nanoreactors for all-stage biofilm associated infection through bacterial cuproptosis-like death and macrophage Re-rousing, *Advan. Mater. (Deerfield Beach, Fla)* 35 (36) (2023) e2303432.
- [9] X. Wang, M. Liu, C. Yu, et al., Biofilm formation: mechanistic insights and therapeutic targets, *Molecul. Biomed.* 4 (1) (2023) 49.
- [10] C.B. Ibberson, J.P. Barraza, A.L. Holmes, et al., Precise spatial structure impacts antimicrobial susceptibility of *S. aureus* in polymicrobial wound infections, *Proc. Natl. Acad. Sci. U. S. A.* 119 (51) (2022) e2212340119.
- [11] C.A. Fux, J.W. Costerton, P.S. Stewart, et al., Survival strategies of infectious biofilms, *Trends Microbiol.* 13 (1) (2005) 34–40.
- [12] J.L. Del Pozo, R. Patel, Clinical practice. Infection associated with prosthetic joints, *N. Engl. J. Med.* 361 (8) (2009) 787–794.
- [13] Tu Zhuolong, Mi Chen, Min Wang, et al., Engineering bioactive M2 macrophage-polarized anti-inflammatory, antioxidant, and antibacterial scaffolds for rapid angiogenesis and diabetic wound repair, *Adv. Funct. Mater.* 31 (30) (2021) 2100924.
- [14] J. Zhu, J. Fan, Y. Xia, et al., Potential therapeutic targets of macrophages in inhibiting immune damage and fibrotic processes in musculoskeletal diseases, *Front. Immunol.* 14 (2023) 1219487.
- [15] K. Zheng, W. Niu, B. Lei, et al., Immunomodulatory bioactive glasses for tissue regeneration, *Acta Biomater.* 133 (2021) 168–186.
- [16] E. Mass, F. Nimmerjahn, K. Kierdorf, et al., Tissue-specific macrophages: how they develop and choreograph tissue biology, *Nat. Rev. Immunol.* 23 (9) (2023) 563–579.
- [17] C.M. Leopold Wager, J.R. Bonifacio, J. Simper, et al., Activation of transcription factor CREB in human macrophages by *Mycobacterium tuberculosis* promotes bacterial survival, reduces NF- κ B nuclear transit and limits phagolysosome fusion by reduced necroptotic signaling, *PLoS Pathog.* 19 (3) (2023) e1011297.
- [18] Thurlow LR, M.L. Hanke, T. Fritz, et al., *Staphylococcus aureus* biofilms prevent macrophage phagocytosis and attenuate inflammation in vivo, *J. Immunol. (Baltimore, Md. : 1950)* 186 (11) (2011) 6585–6596.
- [19] X. Jia, I. Ahmad, R. Yang, et al., Versatile graphene-based photothermal nanocomposites for effectively capturing and killing bacteria, and for destroying bacterial biofilms, *J. Mater. Chem. B* 5 (13) (2017) 2459–2467.
- [20] C. Duchesne, N. Frescaline, O. Blaise, et al., Cold atmospheric plasma promotes killing of *Staphylococcus aureus* by macrophages, *mSphere* (2021) e0021721 null.
- [21] Y.Z. Lu, B. Nayer, S.K. Singh, et al., CGRP sensory neurons promote tissue healing via neutrophils and macrophages, *Nature* 628 (8008) (2024) 604–611.
- [22] X. Zhang, Y. Liu, M. Jiang, et al., Polarization of macrophages to an anti-cancer phenotype through in situ uncaging of a TLR 7/8 agonist using bioorthogonal nanozymes, *Chem. Sci.* 15 (7) (2024) 2486–2494.
- [23] Li Xiaodie, Lan Yufei, Xin Fu, et al., DNA nanomachine-driven chemodynamic therapy against glioblastoma, *Aggregate* 5 (6) (2024) e603.
- [24] Y. Lan, X. Li, B. Liu, et al., Framework nucleic acid-based nanoparticles enhance temozolomide sensitivity in glioblastoma, *Drug Resist. Updates* 76 (2024) 101122.
- [25] Li Xiaodie, Li Lei, Xin Fu, et al., A novel tetrahedral framework nucleic acid-derived chemodynamic therapy agent for effective glioblastoma treatment, *Cell Prolif.* 58 (1) (2025) e13736.
- [26] L. Li, Y. Xie, J. Wang, et al., Biofilm microenvironment-activated multimodal therapy nanoplatforam for effective anti-bacterial treatment and wound healing, *Acta Biomater.* 183 (2024) 221–234.
- [27] Y. Zhang, Q. Liu, C.B. Ma, et al., Point-of-care assay for drunken driving with Pd@Pt core-shell nanoparticles-decorated ploy(vinyl alcohol) aerogel assisted by portable pressure meter, *Theranostics* 10 (11) (2020) 5064–5073.
- [28] Xinyue Kong, Xiangmei Liu, Yufeng Zheng, et al., Graphitic carbon nitride-based materials for photocatalytic antibacterial application, *Mater. Sci. Eng. R Rep.* (2021).
- [29] K.R. Reddy, C.V. Reddy, M.N. Nadagouda, et al., Polymeric graphitic carbon nitride (g-C₃N₄)-based semiconducting nanostructured materials: synthesis methods, properties and photocatalytic applications, *J. Environ. Manag.* 238 (2019) 25–40.
- [30] J.H. Thurston, A.J. Clifford, B.S. Henderson, et al., Development of photoactive g-C₃N₄/Poly(vinyl alcohol) composite hydrogel films with antimicrobial and antibiofilm activity, *ACS Appl. Bio Mater.* 3 (3) (2020) 1681–1689.
- [31] E. Sánchez-López, D. Gomes, G. Esteruelas, et al., Metal-based nanoparticles as antimicrobial agents: an overview, *Nanomaterials* 10 (2) (2020) 292.
- [32] M. Kiarashi, P. Mahamed, N. Ghotbi, et al., Spotlight on therapeutic efficiency of green synthesis metals and their oxide nanoparticles in periodontitis, *J. Nanobiotechnol.* 22 (1) (2024) 21.
- [33] Y. Li, Y. Wang, Y. Ding, et al., A double network composite hydrogel with self-regulating Cu²⁺/luteolin release and mechanical modulation for enhanced wound healing, *ACS Nano* 18 (26) (2024) 17251–17266.
- [34] W. Wang, W. Mo, Z. Hang, et al., Cuproptosis: harnessing transition metal for cancer therapy, *ACS Nano* 17 (20) (2023) 19581–19599.
- [35] Y.L. Wang, J.J. Hu, Sub-100-micron calcium-alginate microspheres: preparation by nitrogen flow focusing, dependence of spherical shape on gas streams and a drug carrier using acetaminophen as a model drug, *Carbohydr. Polym.* 269 (2021) 118262.
- [36] X. Peng, Y. Li, T. Li, et al., Coacervate-derived hydrogel with effective water repulsion and robust underwater bioadhesion promotes wound healing, *Adv. Sci.* 9 (31) (2022) e2203890.
- [37] C. Pu, Y. Wang, Y. Li, et al., Nano-enzyme functionalized hydrogels promote diabetic wound healing through immune microenvironment modulation, *Biomater. Sci.* 12 (15) (2024) 3851–3865.
- [38] Y. Li, M. Yang, Y. Xing, et al., Preparation of carbon-rich g-C₃N₄ nanosheets with enhanced visible light utilization for efficient photocatalytic hydrogen production, *Small* 13 (33) (2017).
- [39] Y. Qiao, J. He, W. Chen, et al., Light-activatable synergistic therapy of drug-resistant bacteria-infected cutaneous chronic wounds and nonhealing keratitis by cupriferous hollow nanoshells, *ACS Nano* 14 (3) (2020) 3299–3315.
- [40] L. Wang, X. Fan, M. Gonzalez Moreno, et al., Photocatalytic quantum dot-armed bioresorbable hydrogel for combating drug-resistant bacterial infection, *Adv. Sci.* 9 (17) (2022) e2105668.
- [41] Q. Jin, G. Xie, X. Cai, et al., Three-dimensional microspheric g-C₃N₄ coupled by Broussonetia papyrifera biochar: facile sodium alginate immobilization and excellent photocatalytic Cr(IV) reduction, *RSC Adv.* 10 (11) (2020) 6121–6128.
- [42] J. Zeng, L. Yang, L. Zeng, et al., Visualizing cancer resistance via nano-quenching and recovery detector of CD44, *NanoBiotechnology* 22 (1) (2024) 452.
- [43] Y. Wu, B. Lv, S. Wang, et al., Study of molecular interaction and texture characteristics of hydrocolloid-mixed alginate microspheres: as a shell to encapsulate multiphase oil cores, *Carbohydr. Polym.* 326 (2024) 121603.
- [44] S. Sugiyama, M. Fujii, K. Fukuta, et al., Preparation of alkaline earth phosphates with sol containing sodium alginate and sodium diphosphate, *J. Colloid Interface Sci.* 295 (1) (2006) 141–147.
- [45] C. Ghoril, E.K. Rodriguez, A. Nazarian, et al., Recent advances in dendritic macromonomers for hydrogel formation and their medical applications, *Biomacromolecules* 17 (4) (2016) 1235–1252.
- [46] Zhao Chengkun, Li Xing, Xiaowen Han, et al., Molecular co-assembled strategy tuning protein conformation for cartilage regeneration, *Nat. Commun.* 15 (1) (2024) 1488.
- [47] M. Sharifiaghdam, E. Shaabani, R. Faridi-Majidi, et al., Macrophages as a therapeutic target to promote diabetic wound healing, *Mol. Ther.* 30 (9) (2022) 2891–2908.
- [48] C. Li, C. Deng, S. Wang, et al., A novel role for the ROS-ATM-Chk2 axis mediated metabolic and cell cycle reprogramming in the M1 macrophage polarization, *Redox Biol.* 70 (2024) 103059.
- [49] X. Yin, Y. Wei, H. Qin, et al., Oxygen tension regulating hydrogels for vascularization and osteogenesis via sequential activation of HIF-1 α and ERK1/2 signaling pathways in bone regeneration, *Biomater. Adv.* 161 (2024) 213893.
- [50] L. Korczak, P. Majewski, D. Iwaniuk, et al., Molecular mechanisms of tigecycline-resistance among Enterobacterales, *Front. Cell. Infect. Microbiol.* 14 (2024) 1289396.
- [51] Z. Wang, J. Chen, Z. You, et al., Advances in mechanisms of biofilm formation and drug resistance of *Staphylococcus aureus*], *Sheng wu gong cheng xue bao = Chin. J. Biotechnol.* 40 (7) (2024) 2038–2051.
- [52] S. Li, D. Sengupta, S. Chien, Vascular tissue engineering: from in vitro to in situ, *Wiley Interdiscip Rev Syst Biol Med* 6 (1) (2014) 61–76.
- [53] B. Li, W. Yang, R. Shu, et al., Antibacterial and angiogenic (2A) bio-heterojunctions facilitate infectious ischemic wound regeneration via an endogenous-exogenous bistimulatory strategy, *Advan. Mater. (Deerfield Beach, Fla)* 36 (6) (2024) e2307613.
- [54] Y. Li, Y. Lu, B. Qiu, et al., Copper-containing titanium alloys promote angiogenesis in irradiated bone through releasing copper ions and regulating immune microenvironment, *Biomater. Adv.* 139 (2022) 213010.